European Journal of Mechanics / A Solids 101 (2023) 105070

Contents lists available at ScienceDirect

European Journal of Mechanics / A Solids

journal homepage: www.elsevier.com/locate/ejmsol

Forcing the silence of the Lamb waves: Uni-directional propagation in structured gyro-elastic strips and networks

G. Carta [a], M.J. Nieves [b,*], M. Brun [a]

[a] University of Cagliari, Department of Mechanical, Chemical and Materials Engineering, Cagliari, 09123, Italy
[b] Keele University, School of Computer Science and Mathematics, Keele, ST5 5BG, UK

ARTICLE INFO

Keywords:
Lamb waves
Mechanical metamaterial
Micro-structured elastic medium
Gyroscopic properties
Non-reciprocity
Energy flux

ABSTRACT

In this paper, we propose an innovative design of an elastic network, which is capable of channelling the energy supplied by an external source towards any of its endpoints, that can be chosen arbitrarily and in advance. This system, named *Mechanical Switching Network* (MSN), consists of an interconnected array of branches, each of which is represented by a lattice strip endowed with gyroscopic spinners. The latter make the system non-reciprocal and, hence, are responsible for the preferential directionality exhibited by the network. We formulate and solve the forced problem for the gyro-elastic strip in the analytical form and compare the derived solutions with the results of independent finite element simulations, showing an excellent agreement. Additionally, we carry out a parametric analysis to evaluate the influence of the main parameters of the system on the uni-directional wave propagation of Lamb waves. We envisage that the proposed model can have important implications in many engineering applications, where control and tunability of guided waves play a key role.

1. Introduction

Propagation of elastic waves in classical continuous waveguides, such as rods or plates, has been studied for more than 150 years, since the seminal works by Pochhammer (Pochhammer, 1876), Rayleigh (Rayleigh, 1888) and Lamb (Lamb, 1917) (see also the review papers by Meleshko et al. (2009, 2010)). In order to take into account the dynamic effects induced by the micro-structure, discrete models for elastic strips have also been developed. In particular, the scalar problem associated with anti-plane shear waves was solved using Chebyshev polynomials in Sharma (2017) for square and triangular lattice waveguides and in Sharma (2018) for honeycomb structures. The presence of a surface with different material properties was analysed in Eremeyev and Sharma (2019), Sharma and Eremeyev (2019). With regards to the vector problem, the dispersive properties of Lamb waves propagating in discrete homogeneous and heterogeneous triangular lattice strips were discussed in Carta et al. (2023), where it was also shown how to create uni-directional waves through mode conversion and selection.

Guided Lamb waves have proved to be useful in many engineering applications, such as Non-Destructive Testing (NTD) methods for the detection of damage in thin-sheet and tubular elements (Su and Ye, 2009), as well as Structural Health Monitoring (SHM) for the automated diagnosis of structural components (Mishra et al., 2015). More recently, carbon nanotubes (having a discrete graphene-like structure) have attracted increasing attention due to their exceptional electrical, mechanical and thermal properties, that can be extremely useful in electronic (Maheswaran and Shanmugavel, 2022), structural reinforcement (Jafari, 2018) and biomedical (Simon et al., 2019) applications.

The possibility to guide Lamb waves in a more efficient and robust way requires the use of non-conventional systems, such as mechanical metamaterials (Zadpoor, 2016; Bertoldi et al., 2017; Kadic et al., 2019; Surjadi et al., 2019). The design of these artificial structures has led to the attainment of novel and surprising phenomena, such as negative refraction (Craster and Guenneau, 2012; Bordiga et al., 2019b; Madine and Colquitt, 2022), invisibility (Brun et al., 2009; Colquitt et al., 2013; O'Neill et al., 2015; Misseroni et al., 2016, 2019; Meirbekova and Brun, 2020; Cassier et al., 2022), filtering and wave attenuation (Martinsson and Movchan, 2003; Miniaci et al., 2021; Bosia et al., 2022; Fantoni et al., 2022), resonant effects (Ma and Sheng, 2016; Tallarico et al., 2017; Dal Corso et al., 2019), inertia amplification (Yilmaz and Hulbert, 2010; Frandsen et al., 2016; Settimi et al., 2021), localisation (Ayzenberg-Stepanenko and Slepyan, 2008; Pal and Ruzzene, 2017; Vila et al., 2017; Haslinger et al., 2018; Bordiga et al., 2019a; Haslinger et al., 2022), bifurcations (Bordiga et al., 2021; Hima et al., 2022), tunability (Gliozzi et al., 2020), and so on.

A special class of mechanical metamaterials is represented by gyroscopic systems. The first model of a gyro-elastic lattice was proposed

* Corresponding author.
E-mail address: m.nieves@keele.ac.uk (M.J. Nieves).

https://doi.org/10.1016/j.euromechsol.2023.105070
Received 16 December 2022; Received in revised form 28 May 2023; Accepted 4 July 2023
Available online 10 July 2023

in Brun et al. (2012), where it was shown that the presence of gyroscopic spinners is capable of altering the filtering and polarisation properties of the lattice. By introducing a doubly-periodic array of gyroscopic spinners, it is even possible to confine the propagation of waves along a straight line, whose direction can be varied by modifying the arrangement of spinners (Carta et al., 2017). Waves can also be forced to travel at the edge or at an interface of a gyroscopic system in one single direction, as demonstrated in Nash et al. (2015), Wang et al. (2015), Garau et al. (2018), Lee et al. (2018), Mitchell et al. (2018), Garau et al. (2019), Carta et al. (2020, 2023). Localised waveforms in a lattice chain with gyroscopic spinners were investigated in Jones et al. (2020), while the gyroscopic coupling of displacements was exploited to design imperfect chiral interfaces in Movchan et al. (2022). Gyroscopes can also be used as stabilisers in structural applications, as demonstrated in Giaccu (2020) for slender monopole towers and in Carta and Nieves (2021) for frames made of beams and columns.

Gyroscopic spinners act as an external bias (Nassar et al., 2020), responsible for breaking time-reversal symmetry and reciprocity. This property of gyroscopic systems was formally proved in Nieves et al. (2020) in relation to the propagation of Rayleigh waves in a lattice half-space. As a consequence, the dynamic response of the system to an external excitation results in a non-symmetric response with respect to the point of application of the loading (Nieves et al., 2021). Successively, Rayleigh waves travelling on the edge of two-dimensional skyrmion lattices in the presence of Lorentz forces were studied in Benzoni et al. (2021) for a semi-infinite plane and in Marijanović et al. (2022) for a finite-size circular domain. Note that the equations of motion of a spinning top are formally analogous to the equations of motion of a Gilbert or Ampére magnetic dipole (Giordano and Déjardin, 2020). In Zhou and Baz (2023), the gyroscopic force was provided by integrating acoustic cavities with piezoelectric diaphragms, acting as pairs of sensors and actuators, that were controlled in order to exhibit the desired non-reciprocal features. In Rakhimzhanova and Brun (2022) a micro-structured system, made of two orthogonal non-linear lattice chains crossing at a point where a single spinner is attached, was proposed with the aim of having a tunable structure where the direction of wave propagation can be selected.

In this paper, we exploit the non-reciprocity induced by gyroscopic spinners, proved in Nieves et al. (2020), to design a network with an internal lattice structure, where the destination of Lamb waves generated by an external excitation can be chosen *a priori*. An example of such a network, which will be denoted as *Mechanical Switching Network* (MSN), is shown in Fig. 1. In this figure, it is clear that the selected destination is the output labelled as B. Each branch of the network is characterised by a parameter, called *effective gyricity* and indicated by Ω^*, which is associated with the properties of the gyroscopic spinners, as specified in the next sections.

The paper is organised as follows. In Section 2, the description of a gyro-elastic lattice strip and the formulation in both the transient and time-harmonic regimes are presented. In Section 3, the dispersion curves for Lamb waves propagating in the gyro-elastic strip are found and discussed. In Section 4, by means of analytical calculations and finite element simulations, it is shown that the proposed system is capable of creating uni-directional waveforms; in addition, using the concept of energy flux, a parametric analysis is performed to determine for which values of the effective gyricity of the spinners and of the frequency of the external load the preferential directionality is more pronounced. In Section 5, the MSN is described in detail, and it is shown how to tune the spinner properties to channel energy from an external source to a prescribed endpoint. Finally, in Section 6, concluding remarks are provided.

2. Gyro-elastic lattice strip under boundary forcing

2.1. Description of the model

We consider an elastic lattice strip as shown in Figs. 2(a) and 2(b), finite in the x_2-direction and of infinite extent in the x_1-direction. The lattice structure is made of periodically-placed point masses arranged in a triangular fashion, having mass m and interconnected by elastic links of stiffness γ and length L. The width of the strip is controlled by the parameter N, with $N > 2$ and $N \in \mathbb{N}$, that defines the number $N + 1$ of horizontal rows possessed by the strip in the x_2-direction.

Each junction of the lattice is connected to a gyroscope that is hinged at its base (see Fig. 2(c)), while the connection at its tip with the mass is such that the spinning motion of the gyroscope is not transferred to the mass. The gyroscope possesses axial symmetry and has length l along the symmetry axis. Additionally, its moment of inertia about this symmetry axis is denoted by I_1, whereas the moments of inertia about the x_1- and x_2-axes are equal and indicated by I_0. Following Brun et al. (2012), Garau et al. (2019), the gyroscopes couple the in-plane displacements of the lattice nodes. The magnitude of the coupling is controlled via a constant quantity called gyricity $\Omega = \dot{\phi}(t) + \dot{\psi}(t)$ (Garau et al., 2019), that represents the sum of the precession and spin rates of the gyroscope during time t in the regime where the lattice nodes undergo small displacements. Further, the gyroscope provides an additional inertial contribution to the mass at the junction, such that the combined effective mass is given by $m^* = m + I_0/l^2$.

From a practical point of view, the elastic lattice can be built connecting a triangular array of spheres by thin elastic rods. The connection between each gyroscope and mass can be fabricated by drilling a cylindrical hole at the bottom of the sphere, where the tip of the gyroscope can be inserted, and making this connection frictionless, such that the mass does not rotate as the gyroscope spins but only translates as the spinner precesses. In the initial configuration, each gyroscope is hinged at the base and its symmetry axis is in the x_3-direction; the spinning motion can be induced by an electric motor, which would keep the spin rate constant during time. In the case that there is a risk of buckling of the spinners due to the weight of the lattice strip, a different design can be suggested, whereby the strip does not lie atop the system of gyroscopes, but is instead suspended by means of cables attached to the ceiling. Alternatively, the gyroscopic lattice can be constructed by employing dc motors and magnets, as in the experimental tests performed in Nash et al. (2015).

We assume that the nodes along the lower and upper boundaries ($n_2 = 0$ and $n_2 = N$, respectively) are harmonically excited by forces that all possess the same frequency ω_0 and whose exact form will be specified later.

To construct the equations governing the dynamic behaviour of the lattice, we introduce the vectors (see also Fig. 2(a))

$$\boldsymbol{a}^{(1)} = (1,0)^{\mathrm{T}}, \quad \boldsymbol{a}^{(2)} = (1/2, \sqrt{3}/2)^{\mathrm{T}} \quad \text{and} \quad \boldsymbol{a}^{(3)} = (-1/2, \sqrt{3}/2)^{\mathrm{T}}, \tag{1}$$

the matrix

$$\boldsymbol{R} = \begin{pmatrix} 0 & 1 \\ -1 & 0 \end{pmatrix}$$

and the discrete spatial variables

$$x_1 = (n_1 + n_2/2)L \quad \text{and} \quad x_2 = \sqrt{3} n_2 L/2, \quad \text{with} \quad n_1, n_2 \in \mathbb{Z}, \ 0 \le n_2 \le N,$$

that describe the positions of the nodes belonging to the strip, each one identified by the multi-index (n_1, n_2). In what follows, we denote the displacements of the nodes in the strip by

$$\boldsymbol{u}^{(n_1,n_2)}(t) = \boldsymbol{u}(x_1, x_2, t).$$

Additionally, in the equations below the dots atop of the dependent variable will be used to represent time derivatives.

2.1.1. Governing equations

Here, we present the equations governing the transient motion of the masses within the gyro-elastic strip.

First, we assume that the nutation angle θ of the gyroscope and its time derivatives are small (see Fig. 2(c)), which implies that the

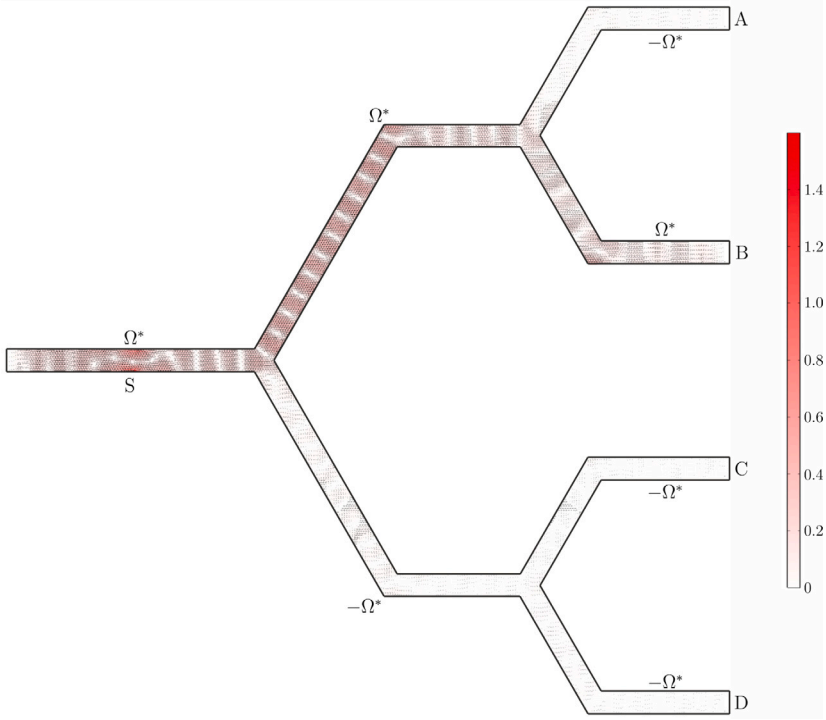

Fig. 1. Illustration of a *Mechanical Switching Network* (MSN), which channels most of the energy coming from the external source S to the output B. The effective gyricity Ω^*, characterising the gyroscopic branches of the network, will be defined in Section 2.

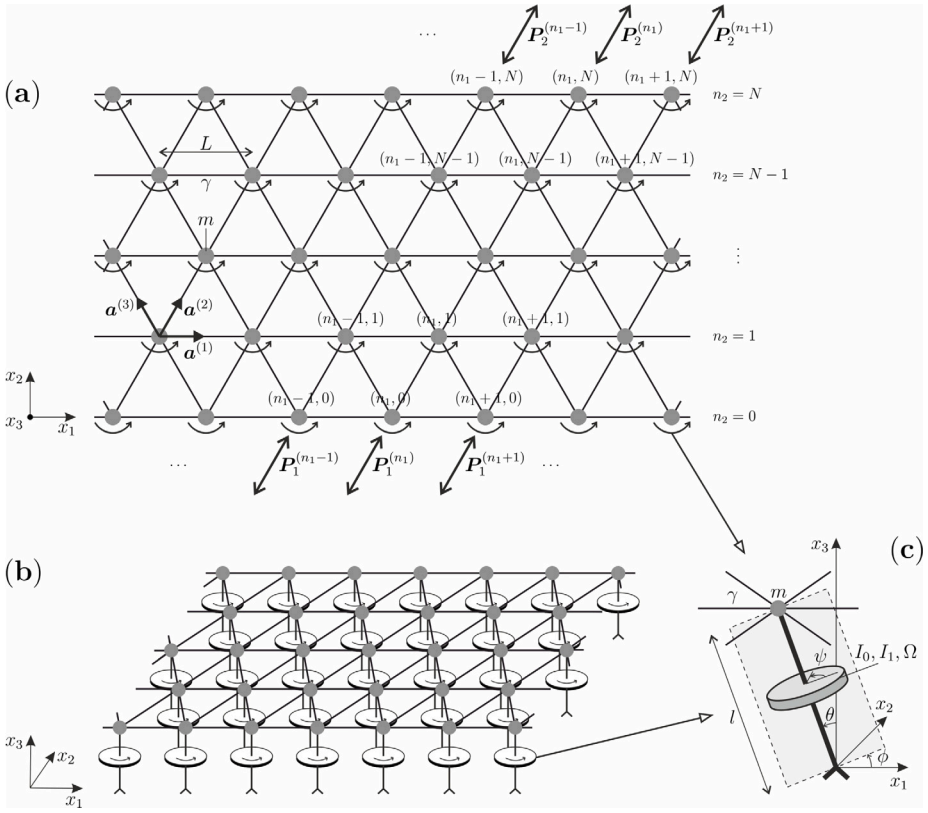

Fig. 2. Discrete elastic strip, consisting of a triangular array of masses m connected by elastic springs of stiffness γ and length L and attached to gyroscopic spinners, characterised by moments of inertia I_0 and I_1 and gyricity Ω: (a) view from above, multi-indexes (n_1, n_2) identify nodes, $\boldsymbol{P}_1^{(n_1)}$ on the lower $(n = 0)$ and $\boldsymbol{P}_2^{(n_1)}$ on the upper $(n = N)$ boundary are the amplitudes of the applied sinusoidal external forces; (b) three-dimensional representation; (c) detail of each gyroscopic spinner, where θ, ϕ and ψ are the three Euler angles, representing the spinner's nutation, precession and spin, respectively.

displacement of the attached mass is also small. Under these conditions, the non-linear equations of motion of the gyroscope can be linearised and the gyricity Ω results to be a constant quantity during the motion. This assumption leads to estimate the gyroscopic effect as a force that is proportional to the velocity of the mass (Garau et al., 2019), as evidenced in the equations below.

Owing to the linear momentum balance, the displacement of the generic node within the lattice bulk characterised by n_1, n_2, with $n_1 \in \mathbb{Z}$ and $0 < n_2 < N$, $n_2 \in \mathbb{N}$, satisfies the equation:

$$\begin{aligned} m^*\ddot{\boldsymbol{u}}^{(n_1,n_2)} = &-\frac{I_0}{l^2}\Omega \boldsymbol{R}\dot{\boldsymbol{u}}^{(n_1,n_2)} + \gamma\Big[\boldsymbol{a}^{(1)}\cdot\left(\boldsymbol{u}^{(n_1+1,n_2)}+\boldsymbol{u}^{(n_1-1,n_2)}-2\boldsymbol{u}^{(n_1,n_2)}\right)\boldsymbol{a}^{(1)} \\ &+\boldsymbol{a}^{(2)}\cdot\left(\boldsymbol{u}^{(n_1,n_2+1)}+\boldsymbol{u}^{(n_1,n_2-1)}-2\boldsymbol{u}^{(n_1,n_2)}\right)\boldsymbol{a}^{(2)} \\ &+\boldsymbol{a}^{(3)}\cdot\left(\boldsymbol{u}^{(n_1-1,n_2+1)}+\boldsymbol{u}^{(n_1+1,n_2-1)}-2\boldsymbol{u}^{(n_1,n_2)}\right)\boldsymbol{a}^{(3)}\Big]. \end{aligned} \tag{2}$$

Along the lower boundary, associated with $n_2 = 0$, the following equations hold:

$$\begin{aligned} m^*\ddot{\boldsymbol{u}}^{(n_1,0)} = &-\frac{I_0}{l^2}\Omega \boldsymbol{R}\dot{\boldsymbol{u}}^{(n_1,0)} + \gamma\Big[\boldsymbol{a}^{(1)}\cdot\left(\boldsymbol{u}^{(n_1+1,0)}+\boldsymbol{u}^{(n_1-1,0)}-2\boldsymbol{u}^{(n_1,0)}\right)\boldsymbol{a}^{(1)} \\ &+\boldsymbol{a}^{(2)}\cdot\left(\boldsymbol{u}^{(n_1,1)}-\boldsymbol{u}^{(n_1,0)}\right)\boldsymbol{a}^{(2)}+\boldsymbol{a}^{(3)}\cdot\left(\boldsymbol{u}^{(n_1-1,1)}-\boldsymbol{u}^{(n_1,0)}\right)\boldsymbol{a}^{(3)}\Big] \\ &+\boldsymbol{P}_1^{(n_1)}\cos(\omega_0 t-\phi_1^{(n_1)}). \end{aligned} \tag{3}$$

On the other hand, the equations of motion along the upper boundary, defined by $n_2 = N$, are expressed by

$$\begin{aligned} m^*\ddot{\boldsymbol{u}}^{(n_1,N)} = &-\frac{I_0}{l^2}\Omega \boldsymbol{R}\dot{\boldsymbol{u}}^{(n_1,N)} + \gamma\Big[\boldsymbol{a}^{(1)}\cdot\left(\boldsymbol{u}^{(n_1+1,N)}+\boldsymbol{u}^{(n_1-1,N)}-2\boldsymbol{u}^{(n_1,N)}\right)\boldsymbol{a}^{(1)} \\ &+\boldsymbol{a}^{(2)}\cdot\left(\boldsymbol{u}^{(n_1,N-1)}-\boldsymbol{u}^{(n_1,N)}\right)\boldsymbol{a}^{(2)} \\ &+\boldsymbol{a}^{(3)}\cdot\left(\boldsymbol{u}^{(n_1+1,N-1)}-\boldsymbol{u}^{(n_1,N)}\right)\boldsymbol{a}^{(3)}\Big]+\boldsymbol{P}_2^{(n_1)}\cos(\omega_0 t-\phi_2^{(n_1)}). \end{aligned} \tag{4}$$

In (3) and (4), the quantities $\boldsymbol{P}_j^{(n_1)}$ and $\phi_j^{(n_1)}$ $(j = 1, 2)$ represent given constant load amplitudes and phases, respectively, of the applied harmonic point forces. Their appearance indicates a harmonic loading that is distributed along both boundaries of the strip amongst the locations of the masses. Thus, the solution of the equations above allows one to determine the response of the strip to a range of distributed loads along the strip's frontiers.

We note that the gyricity Ω, appearing in (2)–(4), will be assumed to be uniform in given regions of the lattice. Accordingly, the same initial conditions will need to be imposed to all the gyroscopes inside a certain region. This can be realised in practice by imposing at $t = 0$ (before an external disturbance generates any elastic wave in the lattice) the same spin rate $\dot{\psi}$ to all the gyroscopes; in this way, the gyricity will have a uniform value ($\Omega = \dot{\psi}(0)$) throughout the same region of the lattice.

2.2. Normalisation

It is convenient to work with non-dimensional quantities. To this aim, we introduce dimensionless displacements:

$$\boldsymbol{u}^{(n_1,n_2)}(t) = L\tilde{\boldsymbol{u}}^{(n_1,n_2)}(\tilde{t}),$$

where $\tilde{\boldsymbol{u}}^{(n_1,n_2)}(\tilde{t}) = \tilde{\boldsymbol{u}}(n_1 + n_2/2, n_2, \tilde{t})$ and $\tilde{t}$ is the dimensionless time defined by $t = \tilde{t}\sqrt{m^*/\gamma}$. In addition, we employ the following normalised quantities, appearing with a tilde:

$$\Omega = \tilde{\Omega}\sqrt{\gamma/m^*}, \quad \omega_0 = \tilde{\omega}_0\sqrt{\gamma/m^*} \quad \text{and} \quad \boldsymbol{P}_j^{(n_1)} = \tilde{\boldsymbol{P}}_j^{(n_1)}\gamma L.$$

Further, we introduce the *effective gyricity* Ω^*, defined by

$$\Omega^* = \tilde{\Omega}I_0/(m^* l^2).$$

In what follows, we drop the tilde associated with the dimensionless quantities for ease of notation.

2.2.1. Dimensionless time-dependent governing equations

We seek the dimensionless displacements of the lattice's particles in the form:

$$\boldsymbol{u}^{(n_1,n_2)}(t) = \mathrm{Re}\left[\boldsymbol{U}^{(n_1,n_2)}(t)e^{\mathrm{i}\omega_0 t}\right],$$

where $\boldsymbol{U}^{(n_1,n_2)}(t) = \boldsymbol{U}(n_1 + n_2/2, n_2, t)$ are complex displacement amplitudes, to be calculated.

Here, we aim to derive the steady-state problem in terms of the discrete Fourier transforms of complex displacement amplitudes. This will be achieved later by taking the limit as $t \to \infty$. As a consequence of the causality principle (Slepyan, 2002), the limiting problem will contain a small dissipation term that allows one to employ techniques from complex function theory to evaluate the displacements of the medium through the inversion of the Fourier transform (see Section 4).

Next, we rewrite the governing Eqs. (2)–(4) in non-dimensional forms and in terms of the displacement amplitudes. For $0 < n_2 < N$, $n_2 \in \mathbb{Z}$, we have

$$\begin{aligned} &\ddot{\boldsymbol{U}}^{(n_1,n_2)} + (2\mathrm{i}\omega_0\boldsymbol{I} + \Omega^*\boldsymbol{R})\dot{\boldsymbol{U}}^{(n_1,n_2)} - \omega_0^2\boldsymbol{U}^{(n_1,n_2)} + \mathrm{i}\omega_0\Omega^*\boldsymbol{R}\boldsymbol{U}^{(n_1,n_2)} \\ = \;& \boldsymbol{a}^{(1)}\cdot\left(\boldsymbol{U}^{(n_1+1,n_2)}+\boldsymbol{U}^{(n_1-1,n_2)}-2\boldsymbol{U}^{(n_1,n_2)}\right)\boldsymbol{a}^{(1)} \\ &+\boldsymbol{a}^{(2)}\cdot\left(\boldsymbol{U}^{(n_1,n_2+1)}+\boldsymbol{U}^{(n_1,n_2-1)}-2\boldsymbol{U}^{(n_1,n_2)}\right)\boldsymbol{a}^{(2)} \\ &+\boldsymbol{a}^{(3)}\cdot\left(\boldsymbol{U}^{(n_1-1,n_2+1)}+\boldsymbol{U}^{(n_1+1,n_2-1)}-2\boldsymbol{U}^{(n_1,n_2)}\right)\boldsymbol{a}^{(3)}. \end{aligned} \tag{5}$$

Conversely, the equations for the nodes along the lower boundary of the strip ($n_2 = 0$) are

$$\begin{aligned} &\ddot{\boldsymbol{U}}^{(n_1,0)} + (2\mathrm{i}\omega_0\boldsymbol{I} + \Omega^*\boldsymbol{R})\dot{\boldsymbol{U}}^{(n_1,0)} - \omega_0^2\boldsymbol{U}^{(n_1,0)} + \mathrm{i}\omega_0\Omega^*\boldsymbol{R}\boldsymbol{U}^{(n_1,0)} \\ = \;& \boldsymbol{a}^{(1)}\cdot\left(\boldsymbol{U}^{(n_1+1,0)}+\boldsymbol{U}^{(n_1-1,0)}-2\boldsymbol{U}^{(n_1,0)}\right)\boldsymbol{a}^{(1)} \\ &+\boldsymbol{a}^{(2)}\cdot\left(\boldsymbol{U}^{(n_1,1)}-\boldsymbol{U}^{(n_1,0)}\right)\boldsymbol{a}^{(2)} \\ &+\boldsymbol{a}^{(3)}\cdot\left(\boldsymbol{U}^{(n_1-1,1)}-\boldsymbol{U}^{(n_1,0)}\right)\boldsymbol{a}^{(3)}+\boldsymbol{P}_1^{(n_1)}e^{-\mathrm{i}\phi_1^{(n_1)}}, \end{aligned} \tag{6}$$

while on the upper boundary ($n_2 = N$) they are given by

$$\begin{aligned} &\ddot{\boldsymbol{U}}^{(n_1,N)} + (2\mathrm{i}\omega_0\boldsymbol{I} + \Omega^*\boldsymbol{R})\dot{\boldsymbol{U}}^{(n_1,N)} - \omega_0^2\boldsymbol{U}^{(n_1,N)} + \mathrm{i}\omega_0\Omega^*\boldsymbol{R}\boldsymbol{U}^{(n_1,N)} \\ = \;& \boldsymbol{a}^{(1)}\cdot\left(\boldsymbol{U}^{(n_1+1,N)}+\boldsymbol{U}^{(n_1-1,N)}-2\boldsymbol{U}^{(n_1,N)}\right)\boldsymbol{a}^{(1)} \\ &+\boldsymbol{a}^{(2)}\cdot\left(\boldsymbol{U}^{(n_1,N-1)}-\boldsymbol{U}^{(n_1,N)}\right)\boldsymbol{a}^{(2)} \\ &+\boldsymbol{a}^{(3)}\cdot\left(\boldsymbol{U}^{(n_1+1,N-1)}-\boldsymbol{U}^{(n_1,N)}\right)\boldsymbol{a}^{(3)}+\boldsymbol{P}_2^{(n_1)}e^{-\mathrm{i}\phi_2^{(n_1)}}. \end{aligned} \tag{7}$$

2.3. Transformed equations of motion

We transform the Eqs. (5)–(7) using the Laplace transform in time t and the discrete Fourier transform in the index n_1. To this end, we introduce the transformed displacement amplitude:

$$\boldsymbol{U}_{n_2}^{\mathrm{LF}}(s,k) = \sum_{n_1=-\infty}^{\infty}\int_0^{\infty}\boldsymbol{U}^{(n_1,n_2)}(t)e^{-st+\mathrm{i}k(n_1+n_2/2)}\mathrm{d}t.$$

Under this transform, we have

$$\left[\boldsymbol{U}^{(n_1+p,n_2+q)}(t)\right]^{\mathrm{LF}} = e^{-\mathrm{i}k(p+q/2)}\boldsymbol{U}_{n_2+q}^{\mathrm{LF}}(s,k).$$

In this case, assuming that the system is initially at rest, Eqs. (5)–(7) take the form:

$$\begin{aligned} [(s+\mathrm{i}\omega_0)^2\boldsymbol{I} + (s+\mathrm{i}\omega_0)\Omega^*\boldsymbol{R}]\boldsymbol{U}_{n_2}^{\mathrm{LF}} = \;& 2\boldsymbol{a}^{(1)}\cdot(\cos(k)-1)\,\boldsymbol{U}_{n_2}^{\mathrm{LF}}\boldsymbol{a}^{(1)} \\ &+\boldsymbol{a}^{(2)}\cdot\left(e^{-\mathrm{i}k/2}\boldsymbol{U}_{n_2+1}^{\mathrm{LF}}+e^{\mathrm{i}k/2}\boldsymbol{U}_{n_2-1}^{\mathrm{LF}}-2\boldsymbol{U}_{n_2}^{\mathrm{LF}}\right)\boldsymbol{a}^{(2)} \\ &+\boldsymbol{a}^{(3)}\cdot\left(e^{\mathrm{i}k/2}\boldsymbol{U}_{n_2+1}^{\mathrm{LF}}+e^{-\mathrm{i}k/2}\boldsymbol{U}_{n_2-1}^{\mathrm{LF}}-2\boldsymbol{U}_{n_2}^{\mathrm{LF}}\right)\boldsymbol{a}^{(3)} \end{aligned} \tag{8}$$

for $0 < n_2 < N$, $n_2 \in \mathbb{Z}$;

$$\begin{aligned} &[(s+\mathrm{i}\omega_0)^2\boldsymbol{I} + (s+\mathrm{i}\omega_0)\Omega^*\boldsymbol{R}]\boldsymbol{U}_0^{\mathrm{LF}} \\ = \;& 2\boldsymbol{a}^{(1)}\cdot(\cos(k)-1)\,\boldsymbol{U}_0^{\mathrm{LF}}\boldsymbol{a}^{(1)}+\boldsymbol{a}^{(2)}\cdot\left(e^{-\mathrm{i}k/2}\boldsymbol{U}_1^{\mathrm{LF}}-\boldsymbol{U}_0^{\mathrm{LF}}\right)\boldsymbol{a}^{(2)} \\ &+\boldsymbol{a}^{(3)}\cdot\left(e^{\mathrm{i}k/2}\boldsymbol{U}_1^{\mathrm{LF}}-\boldsymbol{U}_0^{\mathrm{LF}}\right)\boldsymbol{a}^{(3)}+\frac{\boldsymbol{\Phi}_1(k)}{s} \end{aligned} \tag{9}$$

for $n_2 = 0$; and

$$\begin{aligned}&[(s+\mathrm{i}\omega_0)^2\boldsymbol{I}+(s+\mathrm{i}\omega_0)\Omega^*\boldsymbol{R}]\boldsymbol{U}_N^{\mathrm{LF}}\\ &= 2\boldsymbol{a}^{(1)}\cdot(\cos(k)-1)\,\boldsymbol{U}_N^{\mathrm{LF}}\boldsymbol{a}^{(1)}+\boldsymbol{a}^{(2)}\cdot\left(e^{\mathrm{i}k/2}\boldsymbol{U}_{N-1}^{\mathrm{LF}}-\boldsymbol{U}_N^{\mathrm{LF}}\right)\boldsymbol{a}^{(2)}\\ &\quad+\boldsymbol{a}^{(3)}\cdot\left(e^{-\mathrm{i}k/2}\boldsymbol{U}_{N-1}^{\mathrm{LF}}-\boldsymbol{U}_N^{\mathrm{LF}}\right)\boldsymbol{a}^{(3)}+\frac{\boldsymbol{\Phi}_2(k)}{s}\end{aligned}\tag{10}$$

for $n_2 = N$. We note that the Fourier transforms of the loads on the upper and lower faces of the strip are

$$\boldsymbol{\Phi}_j(k)=\sum_{n_1\in\mathbb{Z}}\boldsymbol{P}_j^{(n_1)}e^{-\mathrm{i}\phi_j^{(n_1)}+\mathrm{i}k(n_1+p_j/2)},\qquad j=1,2,\tag{11}$$

where $p_1 = 0$ and $p_2 = N$.

2.4. The problem in the steady-state regime

We also define the steady-state amplitudes of the displacements of the lattice's masses through the standard formula

$$\mathbf{U}_{n_2}^{\mathrm{F}}(k)=\lim_{s\to+0}s\boldsymbol{U}_{n_2}^{\mathrm{LF}}(s,k),$$

for $n_2 \in \mathbb{Z}$, $0 \le n_2 \le N$.

Multiplying (8)–(10) by s and employing the preceding limit, we retrieve the following equations for the steady-state regime:

$$\begin{aligned}&[(0+\mathrm{i}\omega_0)^2\boldsymbol{I}+(0+\mathrm{i}\omega_0)\Omega^*\boldsymbol{R}]\mathbf{U}_{n_2}^{\mathrm{F}}=2\boldsymbol{a}^{(1)}\cdot(\cos(k)-1)\,\mathbf{U}_{n_2}^{\mathrm{F}}\boldsymbol{a}^{(1)}\\ &+\boldsymbol{a}^{(2)}\cdot\left(e^{-\mathrm{i}k/2}\mathbf{U}_{n_2+1}^{\mathrm{F}}+e^{\mathrm{i}k/2}\mathbf{U}_{n_2-1}^{\mathrm{F}}-2\mathbf{U}_{n_2}^{\mathrm{F}}\right)\boldsymbol{a}^{(2)}\\ &+\boldsymbol{a}^{(3)}\cdot\left(e^{\mathrm{i}k/2}\mathbf{U}_{n_2+1}^{\mathrm{F}}+e^{-\mathrm{i}k/2}\mathbf{U}_{n_2-1}^{\mathrm{F}}-2\mathbf{U}_{n_2}^{\mathrm{F}}\right)\boldsymbol{a}^{(3)}\end{aligned}\tag{12}$$

for $0 < n_2 < N$, $n_2 \in \mathbb{Z}$;

$$\begin{aligned}&[(0+\mathrm{i}\omega_0)^2\boldsymbol{I}+(0+\mathrm{i}\omega_0)\Omega^*\boldsymbol{R}]\mathbf{U}_0^{\mathrm{F}}\\ &=2\boldsymbol{a}^{(1)}\cdot(\cos(k)-1)\,\mathbf{U}_0^{\mathrm{F}}\boldsymbol{a}^{(1)}+\boldsymbol{a}^{(2)}\cdot\left(e^{-\mathrm{i}k/2}\mathbf{U}_1^{\mathrm{F}}-\mathbf{U}_0^{\mathrm{F}}\right)\boldsymbol{a}^{(2)}\\ &+\boldsymbol{a}^{(3)}\cdot\left(e^{\mathrm{i}k/2}\mathbf{U}_1^{\mathrm{F}}-\mathbf{U}_0^{\mathrm{F}}\right)\boldsymbol{a}^{(3)}+\boldsymbol{\Phi}_1(k)\end{aligned}\tag{13}$$

for $n_2 = 0$; and

$$\begin{aligned}&[(0+\mathrm{i}\omega_0)^2\boldsymbol{I}+(0+\mathrm{i}\omega_0)\Omega^*\boldsymbol{R}]\mathbf{U}_N^{\mathrm{F}}\\ &=\boldsymbol{a}^{(1)}\cdot(\cos(k)-1)\,\mathbf{U}_N^{\mathrm{F}}\boldsymbol{a}^{(1)}+\boldsymbol{a}^{(2)}\cdot\left(e^{\mathrm{i}k/2}\mathbf{U}_{N-1}^{\mathrm{F}}-\mathbf{U}_N^{\mathrm{F}}\right)\boldsymbol{a}^{(2)}\\ &+\boldsymbol{a}^{(3)}\cdot\left(e^{-\mathrm{i}k/2}\mathbf{U}_{N-1}^{\mathrm{F}}-\mathbf{U}_N^{\mathrm{F}}\right)\boldsymbol{a}^{(3)}+\boldsymbol{\Phi}_2(k)\end{aligned}\tag{14}$$

for $n_2 = N$. Here, we note that the term $0 + \mathrm{i}\omega_0$ has been retained and represents the limit

$$\lim_{s\to+0}s+\mathrm{i}\omega_0,\tag{15}$$

that is taken with respect to the Laplace transformed quantities and is associated with the causality principle (Slepyan, 2002).

2.5. The solution to the steady-state problem in the interior of the strip

The solutions to the Eqs. (12) are sought in the form

$$\mathbf{U}_{n_2}^{\mathrm{F}}(k)=\boldsymbol{C}\lambda^{n_2},\quad 0<n_2<N,\tag{16}$$

where $\boldsymbol{C}$ and λ are to be determined.

Substitution of (16) into (12) provides the system

$$\mathbf{0}=\boldsymbol{M}\boldsymbol{C},\tag{17}$$

where

$$\boldsymbol{M}=\begin{bmatrix}\cos\left(\frac{k}{2}\right)\left(\lambda+\frac{1}{\lambda}\right)+8\cos^2\left(\frac{k}{2}\right)-10+2\hat{\omega}_0^2 & -\mathrm{i}\sqrt{3}\sin\left(\frac{k}{2}\right)\left(\lambda-\frac{1}{\lambda}\right)-2\mathrm{i}\Omega^*\hat{\omega}_0\\ -\mathrm{i}\sqrt{3}\sin\left(\frac{k}{2}\right)\left(\lambda-\frac{1}{\lambda}\right)+2\mathrm{i}\Omega^*\hat{\omega}_0 & 3\cos\left(\frac{k}{2}\right)\left(\lambda+\frac{1}{\lambda}\right)-6+2\hat{\omega}_0^2\end{bmatrix},\tag{18}$$

with $\hat{\omega}_0 = \omega_0 - \mathrm{i}0$. A non-trivial vector $\boldsymbol{C}$ satisfying (17) exists if λ satisfies the bi-quadratic equation:

$$\left(\lambda+\frac{1}{\lambda}\right)^2-4b\left(\lambda+\frac{1}{\lambda}\right)+4c=0,\tag{19}$$

whose coefficients are

$$b=\left[2\sin^2\left(\frac{k}{2}\right)+1+\frac{2}{3}\hat{\omega}_0^2\right]\cos\left(\frac{k}{2}\right),$$

$$c=\frac{\hat{\omega}_0^2}{3}\left\{\hat{\omega}_0^2-4\left[\sin^2\left(\frac{k}{2}\right)+1\right]-(\Omega^*)^2\right\}+3\sin^2\left(\frac{k}{2}\right)+1.$$

There are four solutions to (19), denoted by λ_j $(1 \le j \le 4)$, with $\lambda_{j+2} = 1/\lambda_j$ $(j = 1, 2)$, such that for $j = 1, 2$:

$$\lambda_j=\frac{\sqrt{g_j+1}-\sqrt{g_j-1}}{\sqrt{g_j+1}+\sqrt{g_j-1}},$$

with

$$g_j=b+(-1)^{j-1}\sqrt{b^2-c}$$

and $|\lambda_j| < 1$. We take all four roots and, using (16) and (17), we construct the transform of the displacements of the lattice's masses as

$$\mathbf{U}_{n_2}^{\mathrm{F}}(k)=\boldsymbol{U}\boldsymbol{\Lambda}^{n_2}\boldsymbol{B}.\tag{20}$$

Here

$$\boldsymbol{U}=[\boldsymbol{U}_0(\lambda_1),\boldsymbol{U}_0(\lambda_2),\boldsymbol{U}_0(\lambda_1^{-1}),\boldsymbol{U}_0(\lambda_2^{-1})],\tag{21}$$

$$\boldsymbol{\Lambda}=\mathrm{diag}\{\lambda_1,\lambda_2,\lambda_1^{-1},\lambda_2^{-1}\}.\tag{22}$$

In addition

$$\boldsymbol{U}_0(\lambda)=\begin{bmatrix}1\\ h_{\Omega^*}(\lambda)\end{bmatrix}\quad\text{and}\quad h_{\Omega^*}(\lambda)=\frac{\mathrm{i}\sqrt{3}\sin\left(\frac{k}{2}\right)\left(\lambda-\frac{1}{\lambda}\right)-2\mathrm{i}\Omega^*\hat{\omega}_0}{3\cos\left(\frac{k}{2}\right)\left(\lambda+\frac{1}{\lambda}\right)-6+2\hat{\omega}_0^2},\tag{23}$$

while $\boldsymbol{B}$ in (20) is a 4×1 coefficient vector depending on the wave number k and that is unknown at this point.

Before proceeding, we note that, according to Carta et al. (2023), via a straightforward rescaling of $\boldsymbol{B}$ by a non-degenerate diagonal matrix, it is possible to rewrite the solution (20) with a representation that embeds terms defined relative to either boundary at $n_2 = 0$ and $n_2 = N$. Applying this procedure yields an updated form of (20), given by

$$\mathbf{U}_{n_2}^{\mathrm{F}}(k)=\boldsymbol{U}\boldsymbol{Y}(n_2)\boldsymbol{D},\tag{24}$$

where

$$\boldsymbol{Y}(n_2)=\mathrm{diag}\{\lambda_1^{n_2},\lambda_2^{n_2},\lambda_1^{N-n_2},\lambda_2^{N-n_2}\},\tag{25}$$

which is used below as it leads to a compact representation of subsequent calculations. In (24), $\boldsymbol{D}$ is an unknown coefficient vector that is determined in the next section using (13) and (14).

2.6. Conditions along the boundaries of the strip and solution to the problem

The aim of this section is to determine the constant vector $\boldsymbol{D}$ in (24).

We note that the solution (24) is subject to (12). Hence, substituting this solution into (13) and (14), one can write down an equivalent, more condensed form of these equations satisfied by (24) which take the form:

$$\boldsymbol{a}^{(2)}\cdot\left(e^{\mathrm{i}k/2}\mathbf{U}_{-1}^{\mathrm{F}}-\mathbf{U}_0^{\mathrm{F}}\right)\boldsymbol{a}^{(2)}+\boldsymbol{a}^{(3)}\cdot\left(e^{-\mathrm{i}k/2}\mathbf{U}_{-1}^{\mathrm{F}}-\mathbf{U}_{n_2}^{\mathrm{F}}\right)\boldsymbol{a}^{(3)}=\boldsymbol{\Phi}_1(k),\tag{26}$$

$$\boldsymbol{a}^{(2)}\cdot\left(e^{-\mathrm{i}k/2}\mathbf{U}_{N+1}^{\mathrm{F}}-\mathbf{U}_N^{\mathrm{F}}\right)\boldsymbol{a}^{(2)}+\boldsymbol{a}^{(3)}\cdot\left(e^{\mathrm{i}k/2}\mathbf{U}_{N+1}^{\mathrm{F}}-\mathbf{U}_N^{\mathrm{F}}\right)\boldsymbol{a}^{(3)}=\boldsymbol{\Phi}_2(k).\tag{27}$$

Using (24) together with the above leads to the following system:

$$\hat{\boldsymbol{Q}}\boldsymbol{D}=\boldsymbol{\Phi}(k),\tag{28}$$

where

$$\boldsymbol{\Phi}(k)=\begin{bmatrix}\boldsymbol{\Phi}_1(k)\\ \boldsymbol{\Phi}_2(k)\end{bmatrix}\quad\text{and}\quad\hat{\boldsymbol{Q}}=\begin{bmatrix}\boldsymbol{Q}_{\Omega}(\lambda_1,\lambda_2) & \boldsymbol{Q}_{\Omega}(\lambda_1^{-1},\lambda_2^{-1})\boldsymbol{K}^N\\ \boldsymbol{X}\boldsymbol{Q}_{-\Omega}(\lambda_1^{-1},\lambda_2^{-1})\boldsymbol{K}^N & \boldsymbol{X}\boldsymbol{Q}_{-\Omega}(\lambda_1,\lambda_2)\end{bmatrix},\tag{29}$$

with

$$\boldsymbol{Q}_\tau(\lambda_1,\lambda_2) = \begin{bmatrix} \frac{\cos\left(\frac{k}{2}\right)-\lambda_1}{2\lambda_1} + \frac{\sqrt{3}\mathrm{i}h_\tau(\lambda_1)\sin\left(\frac{k}{2}\right)}{2\lambda_1} & \frac{\cos\left(\frac{k}{2}\right)-\lambda_2}{2\lambda_2} + \frac{\sqrt{3}\mathrm{i}h_\tau(\lambda_2)\sin\left(\frac{k}{2}\right)}{2\lambda_2} \\ \frac{\sqrt{3}\mathrm{i}\sin\left(\frac{k}{2}\right)}{2\lambda_1} + \frac{3h_\tau(\lambda_1)\left[\cos\left(\frac{k}{2}\right)-\lambda_1\right]}{2\lambda_1} & \frac{\sqrt{3}\mathrm{i}\sin\left(\frac{k}{2}\right)}{2\lambda_2} + \frac{3h_\tau(\lambda_2)\left[\cos\left(\frac{k}{2}\right)-\lambda_2\right]}{2\lambda_2} \end{bmatrix},$$

$$\boldsymbol{K} = \mathrm{diag}\{\lambda_1,\lambda_2\} \quad \text{and} \quad \boldsymbol{X} = \mathrm{diag}\{1,-1\}.$$

Thus, combining (28) with (24) gives the solution for the transformed displacements of the gyro-elastic strip:

$$\mathbf{U}^{\mathrm{F}}_{n_2}(k) = \boldsymbol{U}\boldsymbol{Y}(n_2)\hat{\boldsymbol{Q}}^{-1}\boldsymbol{\Phi}(k)\,. \tag{30}$$

Note that, in the limit when $N \to \infty$, the solution above for the Fourier transformed displacements reduces to that for the problem of Rayleigh waves propagating along the boundary of a half-plane formed from a gyro-elastic lattice (Nieves et al., 2020). Indeed, as $|\lambda_j| < 1$ ($j = 1,2$), in this limit the matrix $\boldsymbol{D}$ becomes a block diagonal (see (29)). Additionally, as $N \to \infty$, only the first diagonal block of $\boldsymbol{Y}$ in (25) remains non-zero. The last limit demonstrates that the influence of the boundary located at $n_2 = N$ on the lattice motion and within the solution (30) becomes absent. Then, when $N \to \infty$, we can take the transformed lattice displacements to be

$$\mathbf{U}^{\mathrm{F}}_{n_2}(k) = [\boldsymbol{U}_0(\lambda_1),\boldsymbol{U}_0(\lambda_2)]\boldsymbol{K}^{n_2}[\boldsymbol{Q}_\Omega(\lambda_1,\lambda_2)]^{-1}\boldsymbol{\Phi}_1(k).$$

2.7. Solution to the steady-state problem

The lattice strip's displacement field in the steady-state regime, defined by

$$\boldsymbol{\mathcal{U}}^{(n_1,n_2)}(t) = \lim_{t\to\infty}\boldsymbol{u}^{(n_1,n_2)}(t),$$

is found by applying the inverse discrete Fourier Transform to (30). The displacements of the lattice's nodes have the form

$$\boldsymbol{\mathcal{U}}^{(n_1,n_2)}(t) = \mathrm{Re}[\mathbf{U}^{(n_1,n_2)}e^{\mathrm{i}\omega_0 t}]\,, \tag{31}$$

where the complex displacement amplitudes are found from

$$\mathbf{U}^{(n_1,n_2)} = \begin{cases} \dfrac{1}{2\pi}\displaystyle\int_{-\pi}^{\pi}\mathbf{U}^{\mathrm{F}}_{n_2}(k)e^{-\mathrm{i}k(n_1+n_2/2)}\mathrm{d}k & \text{if } n_2 \text{ is even,} \\ \dfrac{1}{4\pi}\displaystyle\int_{-2\pi}^{2\pi}\mathbf{U}^{\mathrm{F}}_{n_2}(k)e^{-\mathrm{i}k(n_1+n_2/2)}\mathrm{d}k & \text{if } n_2 \text{ is odd,}. \end{cases} \tag{32}$$

3. Dispersion curves

The dispersion relation, which shows how the radian frequency ω of waves propagating in the strip depends on the wave number k, is found by setting the loading term $\boldsymbol{\Phi}(k) = 0$ in (28), in addition to replacing $\omega_0 - \mathrm{i}0$ by ω, and searching for degenerate values of the matrix $\hat{\boldsymbol{Q}}$ in (28). The dispersion relation is associated with singular points of the integral kernel appearing in (32), owing to the solution (30).

An illustrative example is presented in Fig. 3, where the dispersion diagram for $N = 10$ and $\Omega^* = 0.5$ is shown. The pairs of values of ω and k for which the matrix $\hat{\boldsymbol{Q}}$ in (28) becomes degenerate are represented by dots.

First of all, we point out that the number of dispersion curves is equal to $2(N+1)$ (that is 22 in the present example), since there are $N+1$ rows in the lattice and each node possesses two degrees of freedom. This is analogous to what observed in triangular lattice strips without gyroscopic spinners (Carta et al., 2023). In addition, in Fig. 3 we note that only one dispersion curve departs from the origin of the dispersion diagram, where low-frequency large-wavelength vibrations are characterised by dispersive features (since the relationship between ω and k is not linear). On the other hand, in the non-gyroscopic waveguide a double solution was found at $(k,\omega) = (0,0)$, with dispersion curves characterised by either a linear or quadratic trend in the neighbourhood of the origin (Carta et al., 2023). It is also important to underline that the dispersion diagram in Fig. 3 does not exhibit internal band-gaps; the only stop-band, where waves decay exponentially, is found for $\omega > 2.5118$.

4. Uni-directional propagation in a straight strip

In this section, we present an example of a gyro-elastic lattice strip with 11 rows ($N = 10$), that is loaded by a horizontally acting point force with frequency $\omega_0 = 0.3$ and unit amplitude, located along the lower boundary of the strip. Accordingly, in this case $\boldsymbol{\Phi}_1 = (1,0)^{\mathrm{T}}$ and $\boldsymbol{\Phi}_2 = (0,0)^{\mathrm{T}}$ in (30), which corresponds to the case in (11) when $\boldsymbol{P}_1^{(n_1)} = (1,0)^{\mathrm{T}}e^{\mathrm{i}\phi_1^{(0)}}\delta_{n_1,0}$ and $\boldsymbol{P}_2^{(n_1)} = \boldsymbol{0}$, $n_1 \in \mathbb{Z}$, with $\delta_{m,n}$ being the Kronecker delta.

For an ordinary elastic lattice strip without gyroscopic spinners, it is expected that energy propagates in equal amounts in both directions away from the point of application of the force, as illustrated in Fig. 4(a). Conversely, the presence of gyroscopic spinners can lead to a quasi-perfect uni-directional propagation, as shown in Fig. 4(b) where the chosen value of gyricity is $\Omega^* = 0.5$. The displacement fields in Figs. 4(a) and 4(b) are obtained from (31).

Here, the inversion of the Fourier transform in (32) can be evaluated in a semi-analytic manner. Without the dissipative term in (15), the kernel of (32) possesses simple poles owing to the degeneracies of $\hat{\boldsymbol{Q}}$ that are located along the interval of integration in (32). The dissipation creates a small perturbation in the location of these points, shifting them inside the complex plane associated with k. One can then calculate the asymptotes of the kernel near these simple poles and use these to rewrite the kernel of (32) as function involving all such asymptotes and a bounded integrable function. The latter is easily integrated with standard quadrature routines, whereas the integration of the asymptotes is performed using (i) a contour integral involving the selection of an appropriate contour for different n_1 and n_2 in the complex plane defined by k and (ii) the residue theorem to evaluate the sinusoidal contributions to the integrals that represent the waves propagating in the strip.

The results based on the inversion of the Fourier transform in (31) and (32) are also verified by means of independent finite element computations performed in *Comsol Multiphysics* (version 5.6). The lattice is built in the *Structural Mechanics* module by using truss elements and its domain has normalised base length equal to 200. The gyroscopic effect is implemented by introducing an additional point force at each junction of the truss, that mimics the contribution of the gyroscopes to the motion of the nodes (see the first terms in the right-hand sides of Eqs. (2)–(4)). Further, a region with damping is added near the left and right ends of the domain to create *adaptive absorbing layers* that minimise the effect of reflected waves within the computational window. The response of the system to the point force is determined by carrying out a frequency response analysis. The numerical outcomes are presented in Figs. 4(c) and 4(d) for $\Omega^* = 0$ and $\Omega^* = 0.5$, respectively.

Comparing Figs. 4(a) and 4(c) and Figs. 4(b) and 4(d), we note that there is an excellent agreement between the analytical calculations and the numerical simulations.

4.1. Energy flux in the gyro-elastic strip

Here, we calculate the energy fluxes for the waves propagating to the right and to the left of the lattice strip endowed with gyroscopic spinners, in order to determine situations for when uni-directional wave propagation can be attained.

We consider a finite rectangular domain, with height equal to the width of the strip and base centred at the application point of the external load. Since damping is absent inside the computational

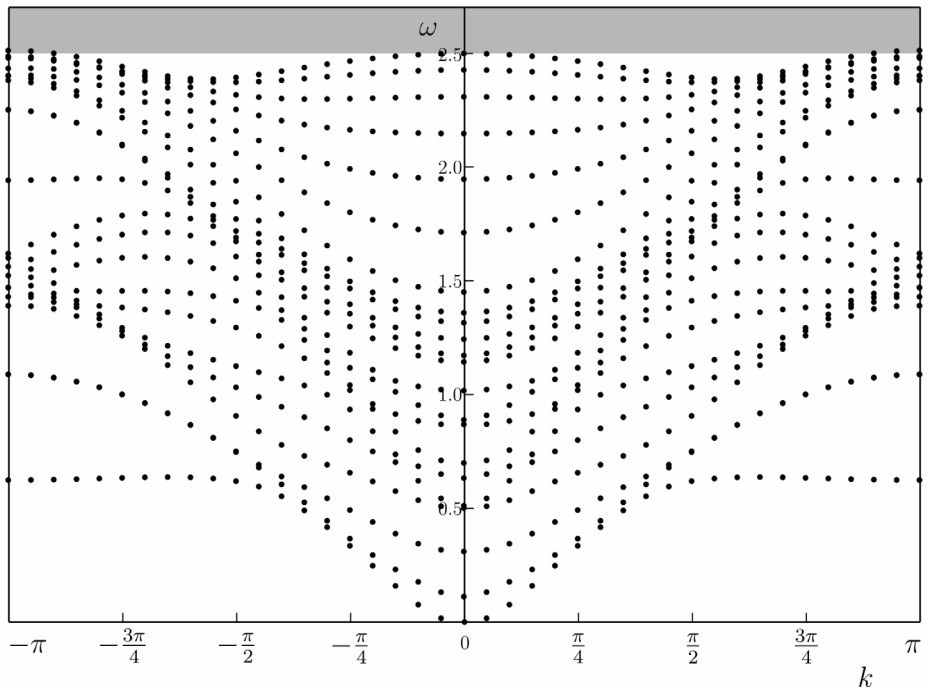

Fig. 3. Dispersion curves for a gyro-elastic lattice strip with 11 rows and effective gyricity $\Omega^* = 0.5$. The semi-infinite stop-band is coloured in grey.

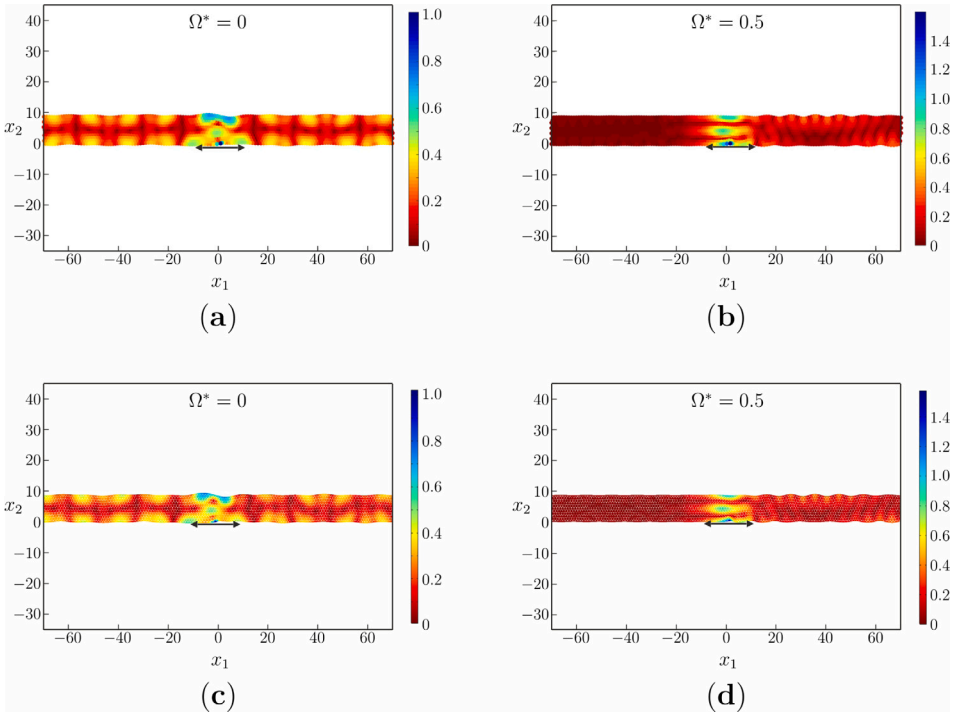

Fig. 4. Displacement field in a discrete strip, infinite in the x_1-direction and consisting of 11 rows in the x_2-direction, subjected to a point force at $(0,0)$ acting in the x_1-direction, having frequency $\omega_0 = 0.3$ and unit amplitude. (a,b) Analytical solutions given by (31); (c,d) numerical results. (a,c) Ordinary strip with $\Omega^* = 0$; (b,d) gyro-elastic strip with $\Omega^* = 0.5$.

domain, the length of the base of the domain is not relevant. If we indicate the external force in the frequency regime by $\boldsymbol{P} = (1,0)^{\mathrm{T}}$ (see Section 4), then the energy input rate is given by

$$W^{(\mathrm{in})} = \frac{1}{2}\mathrm{Re}\left[\boldsymbol{P}\cdot\bar{\boldsymbol{v}}^{(0,0)}\right],$$

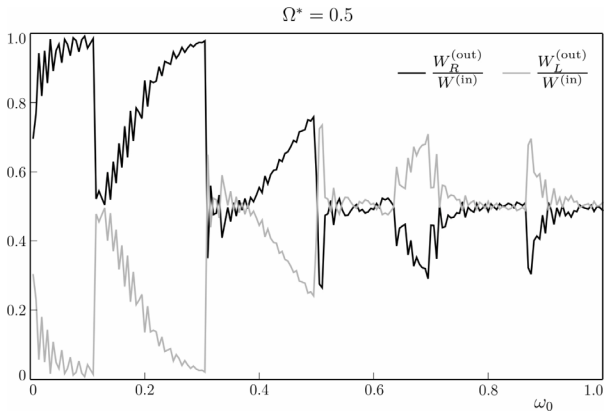

Fig. 5. Ratios of energy flux through the right (black) and left (grey) boundary for different values of the radian frequency ω_0 of the external force and for a fixed gyricity equal to $\Omega^* = 0.5$.

where $\bar{\boldsymbol{v}}^{(n_1,n_2)}$ is the complex conjugate of the velocity. The energy output rates $W_R^{(\text{out})}$ and $W_L^{(\text{out})}$ through the right and left boundaries, respectively, of the domain are determined from the formulae (Brillouin, 1953)

$$W_i^{(\text{out})} = -\frac{1}{2} \sum_{\boldsymbol{n}_j \in D_i} \text{Re}\left[\boldsymbol{F}_{el}^{(\boldsymbol{n}_j)} \cdot \bar{\boldsymbol{v}}^{(\boldsymbol{n}_j)}\right], \quad i = L, R\,,$$

where $\boldsymbol{n}_j$ indicates the generic node in proximity of the boundary and inside the rectangular domain, $\boldsymbol{F}_{el}^{(\boldsymbol{n}_j)}$ denotes the total elastic force provided by the elastic links connected to the node with multi-index $\boldsymbol{n}_j$, and D_i is the set of nodes $\boldsymbol{n}_j$ positioned in the proximity of the boundary. Of course, since the conservation of energy law must hold, the following equality needs to be satisfied:

$$W^{(\text{in})} = W_R^{(\text{out})} + W_L^{(\text{out})}\,. \tag{33}$$

In Fig. 5 we show how the ratios of energy flux propagating to the right ($W_R^{(\text{out})}/W^{(\text{in})}$) and to the left ($W_L^{(\text{out})}/W^{(\text{in})}$) of the domain vary with the radian frequency ω_0 of the external load, when the gyricity is taken as $\Omega^* = 0.5$. First of all, we note that the conservation of energy is verified for any value of the frequency (33). Moreover, it is evident that the energy does not propagate symmetrically to the left and to the right. Furthermore, the energy fluxes strongly depend on ω_0; in particular, at some frequencies there are significant drops in the diagrams, which are associated with zero-group velocity points on the dispersion diagram. Nonetheless, at certain values of the frequency the ratio of energy flowing through the right is close to 1, confirming there exists the possibility to realise uni-directional propagation in the considered system. For instance, when $\omega_0 = 0.3$ (as in Fig. 4(b)), $W_R^{(\text{out})}/W^{(\text{in})} = 0.98$; the same value is obtained with the finite element model in *Comsol Multiphysics*. Finally, we point out that the directional behaviour of energy flux can be reversed by changing the sign of gyricity.

Different values of the gyricity are considered in Fig. 6, namely $\Omega^* = 0.25$ (part (a)) and $\Omega^* = 0.75$ (part (b)). Comparing Figs. 5 and 6, we observe that local maxima are found at different values of the frequency; hence, the phenomenon of uni-directional propagation is easily tunable by varying the gyricity of the spinners. As in Fig. 5, we note that at larger frequencies the strip tends to channel more energy to the left of the source than to the right (for positive gyricity). However, the disparity between the two fluxes in this frequency regime is relatively small in comparison with what is observed in the low-frequency regime, where larger differences in the energy fluxes of left-going and right-going waves are more likely to be achieved.

5. Mechanical switching network (MSN)

The results of Section 4 have suggested the possibility of designing a network of lattice strips, that can route the propagation of elastic waves along a prescribed path and channel the majority of the energy towards a predetermined endpoint (or output) of the network. The choice of the path and, hence, of the output can be varied, depending on the needs of the application. Accordingly, such a device will be referred to as *Mechanical Switching Network* (MSN).

An illustrative example of a MSN is sketched in Fig. 7(a). The primary lattice strip with effective gyricity Ω^*, where the source S is located, is split into two branches, whose effective gyricities are denoted as Ω_1^* (upper branch) and Ω_2^* (lower branch) and are specified below. Each secondary branch is divided into two sub-branches, so that the total number of outputs in the network is equal to 4. The endpoints are indicated by A, B, C and D in Fig. 7(a), and the effective gyricity of each sub-branch is identified with a subscript that refers to the corresponding output. The source S is represented by a horizontal time-harmonic force, with frequency ω_0 and unit amplitude.

The simulations are performed with a finite element model built in *Comsol Multiphysics*. In order to avoid reflections at the ends of the MSN, adaptive absorbing layers (AAL) are inserted, as shown in Fig. 7(a). The effective gyricity of the primary branch and the radian frequency of the point force are taken as $\Omega^* = 0.5$ and $\omega_0 = 0.095$, respectively. This pair of values has been selected in order to achieve a large ratio $W_R^{(\text{out})}/W^{(\text{in})}$ (see Fig. 5).

The effective gyricity of each branch of the MSN is set equal to either Ω^* or $-\Omega^*$, according to the output where it is desired to gather most of the energy introduced by the source. The rule of thumb is to assign to the branches belonging to the chosen path an effective gyricity Ω^* and to the others the equal and opposite value $-\Omega^*$. The switching of the output can be easily implemented by changing the signs of the effective gyricities in the appropriate branches; in practice, this can be realised by reverting the direction of rotation of the spinners.

The results of the numerical simulations are shown in Figs. 7(b)-7(d). In particular, the chosen outputs are A, C and D in parts (b), (c) and (d), respectively. The values of the effective gyricities for the three cases are indicated in the caption of the figure. The situation when energy propagation is directed towards endpoint B has been presented in the Introduction (see Fig. 1). From the figures, it is apparent that the MSN is very efficient at channelling most of the energy towards the selected output. A more quantitative assessment of the proposed design can be achieved by employing the concept of energy flux, discussed in Section 4.1. Following this approach, we have found that in all the four scenarios more than 96.5% of the energy flowing to the right of the source reaches the chosen output. In addition, 2.5% of the energy propagating in the network follows the path of the sub-branch that departs from the same secondary branch as the chosen output, and the residual 1% is divided in almost equal amounts between the remaining sub-branches.

Additional finite element simulations have been carried out in the transient regime to show how elastic waves propagate during time in the four scenarios described above. In the transient regime, the external force has been located in the bottom part of the left end of the primary branch and its expression is given by $\sin(\omega_0 t)$. The outcomes are illustrated in Video 1 - Video 4 of the Supplementary Material. We underline that the simulations have been interrupted when waves reach the prescribed destinations. The videos are a further demonstration of the efficiency of the proposed design.

For comparison, in Video 5 the results of a different simulation are presented, where the effective gyricity is set equal to zero in all branches. In this non-gyroscopic network, the energy is being divided into nearly equal parts when waves impinge on a bifurcation. The slight non-symmetry of the wave motion is due to the non-symmetric position of the source, that acts on the bottom node of the left end of the primary

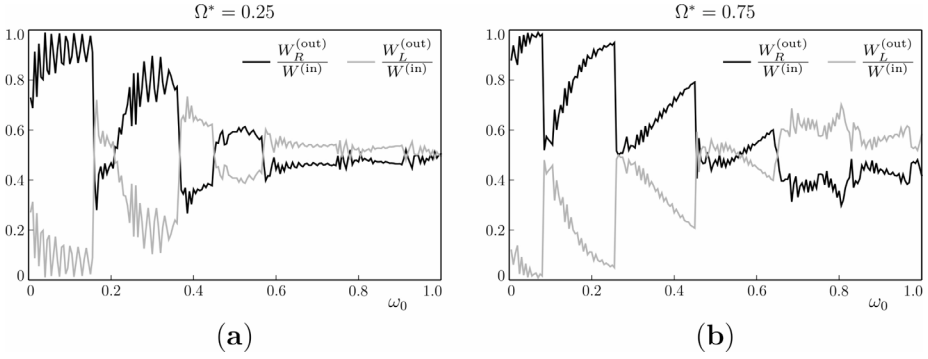

Fig. 6. Same as in Fig. 5, but for different values of gyricity: (a) $\Omega^* = 0.25$; (b) $\Omega^* = 0.75$.

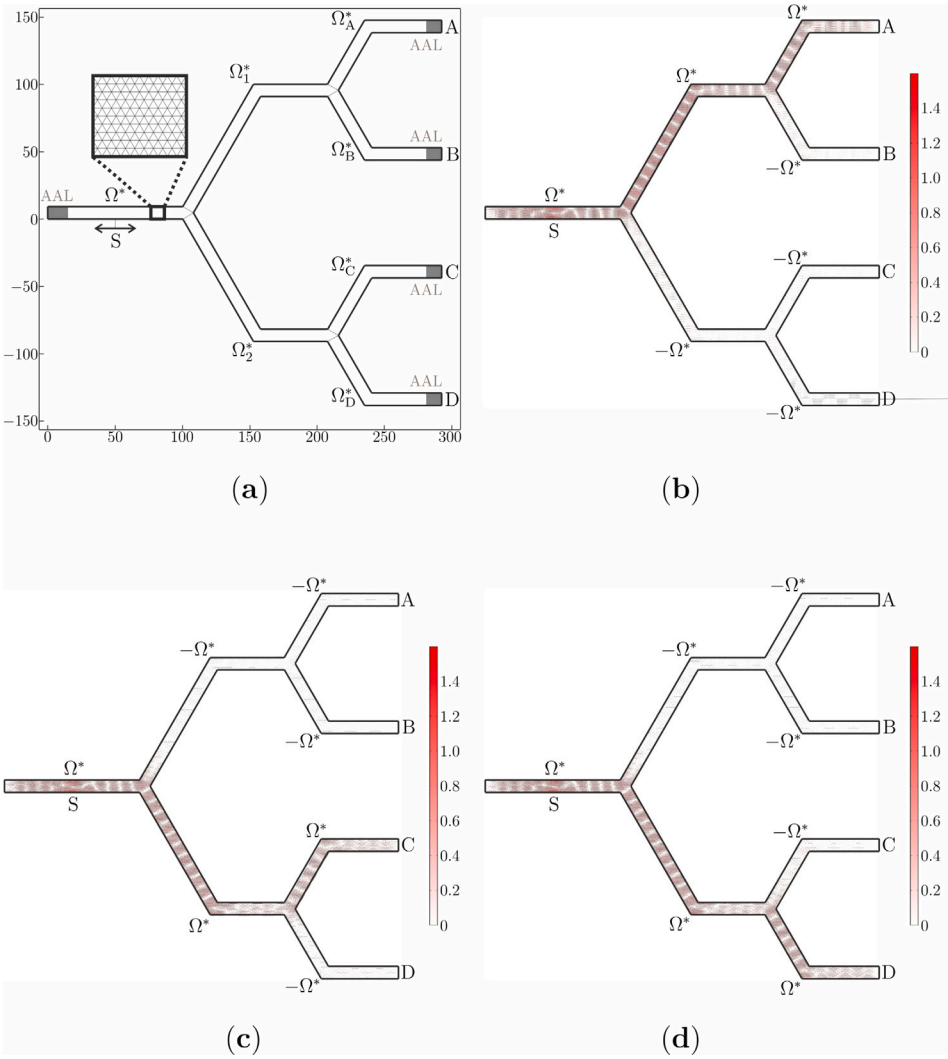

Fig. 7. (a) Schematic drawing of the *Mechanical Switching Network* (MSN), where S is the source and A, B, C, D are the outputs; the effective gyricities in all the branches of the network and the normalised dimensions of the geometry of the numerical model are also indicated. (b-d) Displacement field calculated numerically with different choices of the effective gyricities: (b) $\Omega^* = 0.5$, $\Omega_1^* = \Omega_A^* = \Omega^*$, $\Omega_2^* = \Omega_B^* = \Omega_C^* = \Omega_D^* = -\Omega^*$; (c) $\Omega^* = 0.5$, $\Omega_2^* = \Omega_C^* = \Omega^*$, $\Omega_1^* = \Omega_A^* = \Omega_B^* = \Omega_D^* = -\Omega^*$; (d) $\Omega^* = 0.5$, $\Omega_2^* = \Omega_D^* = \Omega^*$, $\Omega_1^* = \Omega_A^* = \Omega_B^* = \Omega_C^* = -\Omega^*$.

branch. It is apparent that, without the momentum bias introduced by the gyroscopic effect, it is impossible to control wave propagation in a non-gyroscopic network.

6. Conclusions

The non-reciprocity induced by the gyroscopic effect in an elastic lattice has been employed to design a *Mechanical Switching Network*. This MSN is an elastic device capable of redirecting wave propagation along preferential paths in a waveguide network with switching regions.

The design of this device has resulted from analytical study of Lamb waves propagating in a gyro-elastic lattice strip, whose steady-state response and dispersive properties have been identified with the discrete Fourier transform. An excellent agreement between the analytical predictions and those based on finite elements has been demonstrated. This analysis shows the dispersion curves calculated for any branch of the network are symmetric with respect to the wavenumber, as shown in Fig. 3. However, the vibration modes are non-symmetric, as demonstrated in Nieves et al. (2020), and wave propagation also results to be non-symmetric, as illustrated in Fig. 4. This leads to energy flux diagrams which are clearly non-symmetric (see Figs. 5 and 6), so that the response of the system to an external load is different for right-going and left-going waves.

The model proposed in this work is fully tunable, and the tunability can be obtained by simply changing the sign of gyricity in each branch of the network. Analytical and numerical analyses in either the frequency or transient regime show the quality and robustness of the micro-structured system that, after a couple of switches, still redirects 96.5% of the energy towards the designed output port.

We believe that the above design may lead to novel technological applications in Microelectromechanical and Signal Processing Systems.

Declaration of competing interest

The authors declare that they have no known competing financial interests or personal relationships that could have appeared to influence the work reported in this paper.

Data availability

No data was used for the research described in the article.

Acknowledgements

M.J.N. gratefully acknowledges the support of the EU H2020 grant MSCA-RISE-2020-101008140-EffectFact. G.C. and M.B.'s work has been performed under the auspices of GNFM-INDAM.

Appendix A. Supplementary data

Supplementary material related to this article can be found online at https://doi.org/10.1016/j.euromechsol.2023.105070.

References

Ayzenberg-Stepanenko, MV., Slepyan, LI., 2008. Resonant-frequency primitive waveforms andstar waves in lattices. J. Sound Vib. 313, 812–821. http://dx.doi.org/10.1016/j.jsv.2007.11.047.

Benzoni, C., Jeevanesan, B., Moroz, S., 2021. Rayleigh edge waves in two-dimensional crystals with Lorentz forces: From skyrmion crystals to gyroscopic media. Phys. Rev. B 104, 024435. http://dx.doi.org/10.1103/PhysRevB.104.024435.

Bertoldi, K., Vitelli, V., Christensen, J., Van Hecke, M., 2017. Flexible mechanical metamaterials. Nat. Rev. Mater. 2 (17066), http://dx.doi.org/10.1038/natrevmats.2017.66.

Bordiga, G., Cabras, L., Bigoni, D., Piccolroaz, A., 2019a. Free and forced wave propagation in a Rayleigh-beam grid: Flat bands, Dirac cones, and vibration localization vs isotropization. Int. J. Solids Struct. 161, 64–81. http://dx.doi.org/10.1016/j.ijsolstr.2018.11.007.

Bordiga, G., Cabras, L., Piccolroaz, A., Bigoni, D., 2019b. Prestress tuning of negative refraction and wave channeling from flexural sources. Appl. Phys. Lett. 114, 041901. http://dx.doi.org/10.1063/1.5084258.

Bordiga, G., Cabras, L., Piccolroaz, A., Bigoni, D., 2021. Dynamics of prestressed elastic lattices: Homogenization, instabilities, and strain localization. J. Mech. Phys. Solids 146, 104198. http://dx.doi.org/10.1016/j.jmps.2020.104198.

Bosia, F., Dal Poggetto, VF., Gliozzi, AS., Greco, G., Lott, M., Miniaci, M., Ongaro, F., Onorato, M., Seyyedizadeh, SF., Tortello, M., Pugno, NM., 2022. Optimized structures for vibration attenuation and sound control in nature: A review. Matter 5, 3311–3340. http://dx.doi.org/10.1016/j.matt.2022.07.023.

Brillouin, L., 1953. Wave propagation in periodic structures. In: Electric Filters and Crystal Lattices, second ed. Dover Publications Inc.

Brun, M., Guenneau, S., Movchan, AB., 2009. Achieving control of in-plane elastic waves. Appl. Phys. Lett. 94, 061903. http://dx.doi.org/10.1063/1.3068491.

Brun, M., Jones, IS., Movchan, AB., 2012. Vortex-type elastic structured media and dynamic shielding. Proc. R. Soc. Lond. A 468, 3027–3046. http://dx.doi.org/10.1098/rspa.2012.0165.

Carta, G., Colquitt, DJ., Movchan, AB., Movchan, NV., Jones, IS., 2020. Chiral flexural waves in structured plates: Directional localisation and control. J. Mech. Phys. Solids 137, 103866. http://dx.doi.org/10.1016/j.jmps.2020.103866.

Carta, G., Jones, IS., Movchan, NV., Movchan, AB., Nieves, MJ., 2017. "Deflecting elastic prism" and unidirectional localisation for waves in chiral elastic systems. Sci. Rep. 7, 26. http://dx.doi.org/10.1038/s41598-017-00054-6.

Carta, G., Nieves, MJ., 2021. Analytical treatment of the transient motion of inertial beams attached to coupling inertial resonators. J. Engrg. Math. 127, 20. http://dx.doi.org/10.1007/s10665-021-10110-w.

Carta, G., Nieves, MJ., Brun, M., 2023. Lamb waves in discrete homogeneous and heterogeneous systems: Dispersion properties, asymptotics and non-symmetric wave propagation. Eur. J. Mech. A Solids 100, 104695. http://dx.doi.org/10.1016/j.euromechsol.2022.104695.

Carta, G., Nieves, MJ., Brun, M., 2023. Unidirectional interfacial waves in gyroscopic elastic systems. In: Dimitrovová, Z., Biswas, P., Gonçalves, R., Silva, T. (Eds.), Recent Trends in Wave Mechanics and Vibrations. WMVC 2022, In: Mechanisms and Machine Science, vol.125, Springer, Cham, http://dx.doi.org/10.1007/978-3-031-15758-5_117.

Cassier, M., DeGiovanni, T., Guenneau, S., Guevara Vasquez, F., 2022. Active exterior cloaking for the two-dimensional Helmholtz equation with complex wavenumbers and application to thermal cloaking. Phil. Trans. R. Soc. A 380, 20220073. http://dx.doi.org/10.1098/rsta.2022.0073.

Colquitt, DJ., Jones, IS., Movchan, NV., Movchan, AB., Brun, M., McPhedran, RC., 2013. Making waves round a structured cloak: Lattices, negative refraction and fringes. Proc. R. Soc. A 469, 20130218. http://dx.doi.org/10.1098/rspa.2013.0218.

Craster, RV., Guenneau, S., 2012. Acoustic Metamaterials: Negative Refraction, Imaging, Lensing and Cloaking. In: Springer Series in Materials Science, vol.166, Springer, Dordrecht.

Dal Corso, F., Tallarico, D., Movchan, NV., Movchan, AB., Bigoni, D., 2019. Nested Bloch waves in elastic structures with configurational forces. Phil. Trans. R. Soc. A 377, 20190101. http://dx.doi.org/10.1098/rsta.2019.0101.

Eremeyev, VA., Sharma, BL., 2019. Anti-plane surface waves in media with surface structure: Discrete vs. continuum model. Internat. J. Engrg. Sci. 143, 33–38. http://dx.doi.org/10.1016/j.ijengsci.2019.06.007.

Fantoni, F., Bosco, E., Bacigalupo, A., 2022. Multifield nested metafilters for wave propagation control. Extreme Mech. Lett. 56, 101885. http://dx.doi.org/10.1016/j.eml.2022.101885.

Frandsen, NM., Bilal, OR., Jensen, JS., Hussein, MI., 2016. Inertial amplification of continuous structures: Large band gaps from small masses. J. Appl. Phys. 119 (12), 124902. http://dx.doi.org/10.1063/1.4944429.

Garau, M., Carta, G., Nieves, MJ., Jones, IS., Movchan, NV., Movchan, AB., 2018. Interfacial waveforms in chiral lattices with gyroscopic spinners. Proc. R. Soc. Lond. Ser. A Math. Phys. Eng. Sci. 474, 20180132. http://dx.doi.org/10.1098/rspa.2018.0132.

Garau, M., Nieves, MJ., Carta, G., Brun, M., 2019. Transient response of a gyro-elastic structured medium: Unidirectional waveforms and cloaking. Int. J. Eng. Sci. 143, 115–141. http://dx.doi.org/10.1016/j.ijengsci.2019.05.007.

Giaccu, GF., 2020. Modeling a gyroscopic stabilizer for the improvement of the dynamic performances of slender monopole towers. Eng. Struct. 215, 110607. http://dx.doi.org/10.1016/j.engstruct.2020.110607.

Giordano, S., Déjardin, P-M., 2020. Derivation of magnetic inertial effects from the classical mechanics of a circular current loop. Phys. Rev. B 102, 214406. http://dx.doi.org/10.1103/PhysRevB.102.214406.

Gliozzi, AS., Miniaci, M., Chiappone, A., Bergamini, A., Morin, B., Descrovi, E., 2020. Tunable photo-responsive elastic metamaterials. Nature Commun. 11, 2576. http://dx.doi.org/10.1038/s41467-020-16272-y.

Haslinger, SG., Frecentese, S., Carta, G., 2022. Localized waves in elastic plates with perturbed honeycomb arrays of constraints. Phil. Trans. R. Soc. A 380, 20210404. http://dx.doi.org/10.1098/rsta.2021.0404.

Haslinger, SG., Jones, IS., Movchan, NV., Movchan, AB., 2018. Localization in semi-infiniteherringbone waveguides. Proc. R. Soc. Lond. Ser. A Math. Phys. Eng. Sci. 474, 20170590. http://dx.doi.org/10.1098/rspa.2017.0590.

Hima, N., Bigoni, D., Dal Corso, F., 2022. Buckling versus unilateral constraint for a multistable metamaterial element. Phil. Trans. R. Soc. A 380, 20220021. http://dx.doi.org/10.1098/rsta.2022.0021.

Jafari, S., 2018. 2 - engineering applications of carbon nanotubes. In: Rafiee, Roham (Ed.), Micro and Nano Technologies, Carbon Nanotube-Reinforced Polymers. Elsevier, pp. 25–40. http://dx.doi.org/10.1016/B978-0-323-48221-9.00002-9.

Jones, IS., Movchan, NV., Movchan, AB., 2020. Two-dimensional waves in a chiral elastic chain: Dynamic green's matrices and localised defect modes. Q. J. Mech. Appl. Math. 73 (4), 305–328. http://dx.doi.org/10.1093/qjmam/hbaa014.

Kadic, M., Milton, GW., Van Hecke, M., Wegener, M., 2019. 3D metamaterials. Nat. Rev. Phys. 1, 198–210. http://dx.doi.org/10.1038/s42254-018-0018-y.

Lamb, H., 1917. On waves in an elastic plate. Proc. R. Soc. Lond. A 93, 114–128. http://dx.doi.org/10.1098/rspa.1917.0008.

Lee, CH., Li, G., Jin, G., Liu, Y., Zhang, X., 2018. Topological dynamics of gyroscopic and floquet lattices from Newton's laws. Phys. Rev. B 97, 085110. http://dx.doi.org/10.1103/PhysRevB.97.085110.

Ma, G., Sheng, P., 2016. Acoustic metamaterials: From local resonances to broad horizons. Sci. Adv. 2 (2), e1501595. http://dx.doi.org/10.1126/sciadv.1501595.

Madine, KH., Colquitt, DJ., 2022. Negative refraction and mode trapping of flexural-torsional waves in elastic lattices. Phil. Trans. R. Soc. A 380, 20210379. http://dx.doi.org/10.1098/rsta.2021.0379.

Maheswaran, R., Shanmugavel, BP., 2022. A critical review of the role of carbon nanotubes in the progress of next-generation electronic applications. J. Electron. Mater. 51, 2786–2800. http://dx.doi.org/10.1007/s11664-022-09516-8.

Marijanović, F., Moroz, S., Jeevanesan, B., 2022. Rayleigh waves and cyclotron surface modes of gyroscopic metamaterials. Phys. Rev. B 106, 024308. http://dx.doi.org/10.1103/PhysRevB.106.024308.

Martinsson, PG., Movchan, AB., 2003. Vibrations of lattice structures and phononic band gaps. Q. J. Mech. Appl. Math. 56, 45–64. http://dx.doi.org/10.1093/qjmam/56.1.45.

Meirbekova, B., Brun, M., 2020. Control of elastic shear waves by periodic geometric transformation: Cloaking, high reflectivity and anomalous resonances. J. Mech. Phys. Solids 137, 103816. http://dx.doi.org/10.1016/j.jmps.2019.103816.

Meleshko, VV., Bondarenko, AA., Dovgiy, SA., Trofimchuk, AN., van Heijst, GJF., 2009. Elastic waveguides: History and the state of the art I. J. Math. Sci. 162, 99–120. http://dx.doi.org/10.1007/s10958-009-9623-8.

Meleshko, VV., Bondarenko, AA., Trofimchuk, AN., Abasov, RZ., 2010. Elastic waveguides: History and the state of the art, II. J. Math. Sci. 167, 197–216. http://dx.doi.org/10.1007/s10958-010-9915-z.

Miniaci, M., Kherraz, N., Cröenne, C., Mazzotti, M., Morvaridi, M., Gliozzi, AS., Onorato, M., Bosia, F., Pugno, NM., 2021. Hierarchical large-scale elastic metamaterials for passive seismic wave mitigation. EPJ Appl. Metamat. 8 (14), http://dx.doi.org/10.1051/epjam/2021009.

Mishra, S., Kumar, A., Mishra, RK., Sharma, S., Singh, S., 2015. Structural health monitoring and propagation of Lamb waves to identification of crack. Mater. Today Proc. 2 (4–5), 1833–1840. http://dx.doi.org/10.1016/j.matpr.2015.07.122.

Misseroni, D., Colquitt, DJ., Movchan, AB., Movchan, NV., Jones, IS., 2016. Cymatics for the cloaking of flexural vibrations in a structured plate. Sci. Rep. 6 (23929), http://dx.doi.org/10.1038/srep23929.

Misseroni, D., Movchan, AB., Bigoni, D., 2019. Omnidirectional flexural invisibility of multiple interacting voids in vibrating elastic plates. Proc. R. Soc. Lond. Ser. A Math. Phys. Eng. Sci. 475, 20190283. http://dx.doi.org/10.1098/rspa.2019.0283.

Mitchell, NP., Nash, LM., Irvine, WTM., 2018. Tunable band topology in gyroscopic lattices. Phys. Rev. B 98, 174301. http://dx.doi.org/10.1103/PhysRevB.98.174301.

Movchan, AB., Movchan, NV., Jones, IS., Milton, GW., Nguyen, H-M., 2022. Frontal waves and transmissions for temporal laminates and imperfect chiral interfaces. Phil. Trans. R. Soc. A 380, 20210385. http://dx.doi.org/10.1098/rsta.2021.0385.

Nash, LM., Kleckner, D., Read, A., Vitelli, V., Turner, AM., Irvine, WTM., 2015. Topological mechanics of gyroscopic metamaterials. Proc. Natl. Acad. Sci. 112, 14495–14500. http://dx.doi.org/10.1073/pnas.1507413112.

Nassar, H., Yousefzadeh, B., Fleury, R., Ruzzene, M., Alù, A., Daraio, C., Norris, AN., Huang, G., Haberman, MR, 2020. Nonreciprocity in acoustic and elastic materials. Nat. Rev. Mater. 5, 667–685. http://dx.doi.org/10.1038/s41578-020-0206-0.

Nieves, MJ., Carta, G., Pagneux, V., Brun, M., 2020. Rayleigh waves in micro-structured elastic systems: Non-reciprocity and energy symmetry breaking. Int. J. Eng. Sci. 156, 103365. http://dx.doi.org/10.1016/j.ijengsci.2020.103365.

Nieves, MJ., Carta, G., Pagneux, V., Brun, M., 2021. Directional control of Rayleigh wave propagation in an elastic lattice by gyroscopic effects. Front. Mater. 7, 602960. http://dx.doi.org/10.3389/fmats.2020.602960.

O'Neill, J., Selsil, Ö, McPhedran, RC., Movchan, AB., Movchan, NV., 2015. Active cloaking of inclusions for flexural waves in thin elastic plates. Q. J. Mech. Appl. Math. 68 (3), 263–288. http://dx.doi.org/10.1093/qjmam/hbv007.

Pal, RK., Ruzzene, M., 2017. Edge waves in plates with resonators: An elastic analogue of thequantum valley Hall effect. New J. Phys. 19, 025001. http://dx.doi.org/10.1088/1367-2630/aa56a2.

Pochhammer, L., 1876. Über die Fortpflanzungsgeschwindigkeiten kleiner Schwingungen in einem unbegrenzten isotropen Kreiscylinder. J. Reine Angew. Math. 81, 324–336. http://dx.doi.org/10.1515/crll.1876.81.324.

Rakhimzhanova, A., Brun, M., 2022. Direction-selective non-reciprocal mechanical energy splitter. Phil. Trans. R. Soc. A 380, 20210372. http://dx.doi.org/10.1098/rsta.2021.0372.

Rayleigh, Lord, 1888. On the free vibrations of an infinite plate of homogeneous isotropic elastic matter. Proc. London Math. Soc. 20, 225–237. http://dx.doi.org/10.1112/plms/s1-20.1.225.

Settimi, V., Lepidi, M., Bacigalupo, A., 2021. Nonlinear dispersion properties of one-dimensional mechanical metamaterials with inertia amplification. Int. J. Mech. Sci. 201, 106461. http://dx.doi.org/10.1016/j.ijmecsci.2021.106461.

Sharma, BL., 2017. On linear waveguides of square and triangular lattice strips: An application of Chebyshev polynomials. Sādhanā 42, 901–927. http://dx.doi.org/10.1007/s12046-017-0646-4.

Sharma, BL., 2018. On linear waveguides of Zigzag honeycomb lattice. Waves Random Complex Media 28 (1), 96–138. http://dx.doi.org/10.1080/17455030.2017.1331061.

Sharma, BL., Eremeyev, VA., 2019. Wave transmission across surface interfaces in lattice structures. Int. J. Eng. Sci. 145, 103173. http://dx.doi.org/10.1016/j.ijengsci.2019.103173.

Simon, J., Flahaut, E., Golzio, M., 2019. Overview of carbon nanotubes for biomedical applications. Mater. (Basel) 12 (4), 624. http://dx.doi.org/10.3390/ma12040624.

Slepyan, LI., 2002. Models and phenomena in fracture mechanics. In: Foundations of Engineering Mechanics. Springer-Verlag, Berlin Heidelberg.

Su, Z., Ye, L., 2009. Identification of Damage using Lamb Waves: From Fundamentals to Applications. In: Lec. Notes Appl. Comp. Mech., vol. 48, Springer, Switzerland, http://dx.doi.org/10.1007/978-1-84882-784-4.

Surjadi, JU., Gao, L., Du, H., Li, X., Xiong, X., Fang, NX., Lu, Y., 2019. Mechanical metamaterials and their engineering applications. Adv. Eng. Mat. 21 (3), 1800864. http://dx.doi.org/10.1002/adem.201800864.

Tallarico, D., Movchan, NV., Movchan, AB., Colquitt, DJ., 2017. Tilted resonators in a triangular elastic lattice: Chirality, Bloch waves and negative refraction. J. Mech. Phys. Solids 103, 236–256. http://dx.doi.org/10.1016/j.jmps.2017.03.007.

Vila, J., Pal, RK., Ruzzene, M., 2017. Observation of topological valley modes in an elastic hexagonal lattice. Phys. Rev. B 96, 134307. http://dx.doi.org/10.1103/PhysRevB.96.134307.

Wang, P., Lu, L., Bertoldi, K., 2015. Topological phononic crystals with one-way elastic edge waves. Phys. Rev. Lett. 115, 104302. http://dx.doi.org/10.1103/PhysRevLett.115.104302.

Yilmaz, C., Hulbert, G., 2010. Theory of phononic gaps induced by inertial amplification in finite structures. Phys. Lett. A 374 (34), 3576–3584. http://dx.doi.org/10.1016/j.physleta.2010.07.001.

Zadpoor, AA., 2016. Mechanical meta-materials. Mater. Horiz 3, 371–381. http://dx.doi.org/10.1039/C6MH00065G.

Zhou, H., Baz, A., 2023. A simple configuration of an actively synthesized gyroscopic-nonreciprocal acoustic metamaterial. ASME J. Vib. Acoust. 145 (2), 021004. http://dx.doi.org/10.1115/1.4055103.